ARTICLE

Room-Temperature Ferromagnetism with Strong Spin−Orbit Coupling Achieved in CaRuO$_3$ Interfacial Phase via Magnetic Proximity Effect

Jie Zheng,[∇] Jing Zhang,[∇] Sheng Cheng, Wenxiao Shi, Mengqin Wang, Zhe Li, Yunzhong Chen, Fengxia Hu, Baogen Shen, Yuansha Chen,* Tao Zhu,* and Jirong Sun*
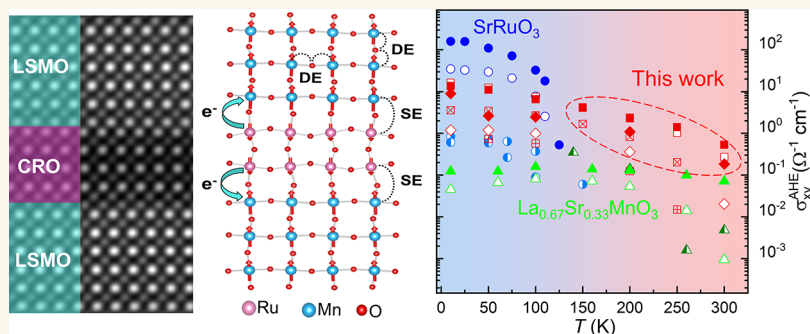
Read Online

ACCESS | Metrics & More | Article Recommendations | Supporting Information

ABSTRACT: Recently, theoretical and experimental research predicted that ferromagnets with strong spin−orbit coupling (SOC) could serve as spin sources with dramatically enhanced spin−orbit torque (SOT) efficiency due to the combination of spin Hall effect and anomalous Hall effect (AHE), presenting potential advantages over conventional nonmagnetic heavy metals. However, materials with a strong SOC and room-temperature ferromagnetism are rare. Here, we report on a ferromagnetic (FM) interfacial phase with Curie temperature exceeding 300 K in the heavy transition-metal oxide CaRuO$_3$, in proximity to La$_{0.67}$Sr$_{0.33}$MnO$_3$. Electron energy loss and polarized neutron reflectometry spectra reveal the strong charge transfer from Ru to Mn at the interface, triggering antiferromagnetic exchange interactions between interfacial Ru/Mn ions and thus transferring magnetic order from La$_{0.67}$Sr$_{0.33}$MnO$_3$ to CaRuO$_3$. An obvious advantage of such interfacial phase is the enhanced anomalous Hall effect at temperatures from 150 to 300 K. Compared to the most promising room-temperature ferromagnetic oxide La$_{0.67}$Sr$_{0.33}$MnO$_3$, the anomalous Hall conductivity σ_{xy}^{AHE} (or anomalous Hall angle θ_H) of CaRuO$_3$/La$_{0.67}$Sr$_{0.33}$MnO$_3$ superlattices is increased by 30 (or 31) times at 150 K and 10 (or 3) times at 300 K. This work demonstrates a special approach for inducing ferromagnetism in heavy transition-metal oxides with strong SOC, offering promising prospects for all-oxide-based spintronic applications.

KEYWORDS: oxide heterostructure, interfacial ferromagnetism, magnetic proximity effect, spin−orbit coupling, antiferromagnetic interaction

INTRODUCTION

The utilization of spin−orbit torque (SOT) to generate spin current and thus electrically switch the magnetization of a ferromagnet is one of the central themes of spintronics.[1−8] In general, SOT derives from the spin Hall effect (SHE) of nonmagnetic heavy metals with strong spin−orbit coupling (SOC), such as Pt and Ta.[5,9−12] Charge-to-spin conversion arising from SHE presents the mutually orthogonal geometric
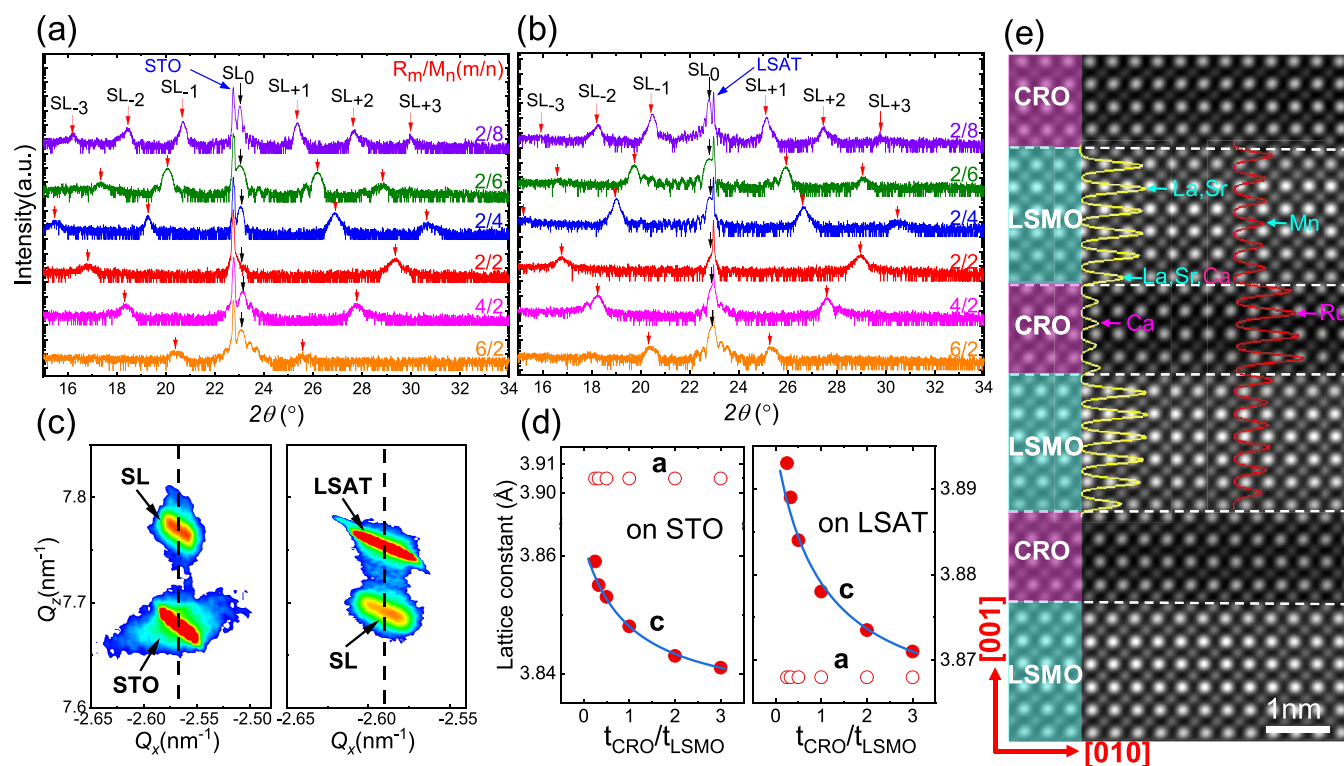
Figure 1. Structural characterization of CRO/LSMO SLs. (a) High-resolution $\theta-2\theta$ patterns of R_m/M_n SLs on STO and (b) LSAT. SL_0 represents the (001) main peak, while SL_{-1}, SL_{+1}, SL_{-2}, SL_{+2}, SL_{-3}, and SL_{+3} represent the satellite peaks. (c) RSM around the pseudocubic (103) reflection for the R_2/M_8 SLs on STO or LSAT substrate, respectively. (d) Out-of-plane and in-plane lattice constants as functions of the relative thickness of the CRO layer (defined as t_{CRO}/t_{LSMO}) for the SLs on STO (left panel) or LSAT (right panel) substrates, deduced from the XRD and RSM results. The blue lines are the calculated out-of-plane lattice constants adopting the formula $c_{SL} = (m \times c_{CRO} + n \times c_{LSMO})/(m + n)$, where c_{CRO} and c_{LSMO} represent the c-axis lattice constants of CRO and LSMO sublayers. (e) High-angle annular dark-field (HAADF) image of the cross section of the R_4/M_6 SL, recorded along the [100] zone axis. The interface between CRO and LSMO is denoted by the dashed horizontal lines marked in white.

configuration for the applied electric field (E), spin flow, and spin polarization.[9,13,14] Specifically, an in-plane charge current flowing along the x-axis generates a spin current flowing toward the film normal (z direction) with spin polarization along the in-plane y-axis. In this setup, to switch the perpendicular magnetization of SOT devices, an auxiliary magnetic field is needed to break the in-plane symmetry, strongly hampering the demand for all-electrical control.[15] Recently, it has been theoretically predicted and experimentally demonstrated that the anomalous Hall effect (AHE) of ferromagnets could also be used for magnetization switching.[13,14,16,17] Replacing the nonmagnetic heavy metal layer with a ferromagnetic (FM) layer with strong SOC can dramatically enhance the efficiency of SOT due to the combined effects of SHE and AHE.[17] Moreover, using the AHE as a spin current source enables control over the orientation of the injected spins and hence the torques, showing potential advantages in the reliable switching of perpendicular ferromagnets.[13,14]

However, FM materials that simultaneously possess strong SOC, a Curie temperature (T_C) above room temperature, and excellent metallicity are scarce. Ordinary FM oxides composed of 3d transition metals exhibit very weak SOC and, consequently, a small AHE. In contrast, 4d/5d transition-metal oxides with strong SOC, such as $CaRuO_3$ (CRO), $SrIrO_3$, and $CaIrO_3$, are usually paramagnetic (PM) due to the weak electron correlation.[18–22] $SrRuO_3$ is an exception, exhibiting both FM and strong SOC, but its T_C of ~160 K falls short of meeting the requirements for room-temperature

applications.[23,24] In this context, considerable research effort has been devoted to developing oxide materials with strong SOC and room-temperature ferromagnetism.[25–30] FM ordering has been induced in PM CRO or $SrIrO_3$ layers via coupled tilting/rotation of the RuO_6 or IrO_6 octahedra when combined with $SrTiO_3$ (STO) or $CaTiO_3$ layers. However, the highest T_C was only 155–170 K.[25–27] Additionally, the magnetic proximity effect at the interface between a PM and an FM oxide can also induce magnetic order in the PM layer. This phenomenon is explained by interfacial exchange interactions based on the Goodenough–Kanamori–Anderson rules.[31–33] For example, the emergence of an FM phase in the PM $SrIrO_3$ layer in proximity to $LaMnO_3$, $SrMnO_3$, or $LaCoO_3$ layer has been reported.[28–30] However, the achieved T_C (<180 K) is still far below room temperature. A survey of the literature reveals that despite extensive investigations, no FM oxides have been obtained so far that exhibit strong SOC, near-room-temperature T_C, and good metallicity.

Here, we report on an FM interfacial phase with a T_C up to 300 K and strong SOC in the CRO/$La_{0.67}Sr_{0.33}MnO_3$ (LSMO) superlattices. Polarized neutron reflectometry (PNR) results confirm the room-temperature ferromagnetism of the CRO layer with an average magnetic moment of ~0.3 μ_B/Ru, which is antiferromagnetically coupled to the LSMO layer. Electron energy loss spectra (EELS) and X-ray magnetic dichroism spectra (XMCD) further reveal the strong charge transfer from Ru to Mn at the interface, triggering antiferromagnetic exchange interactions between interfacial Ru/Mn ions and
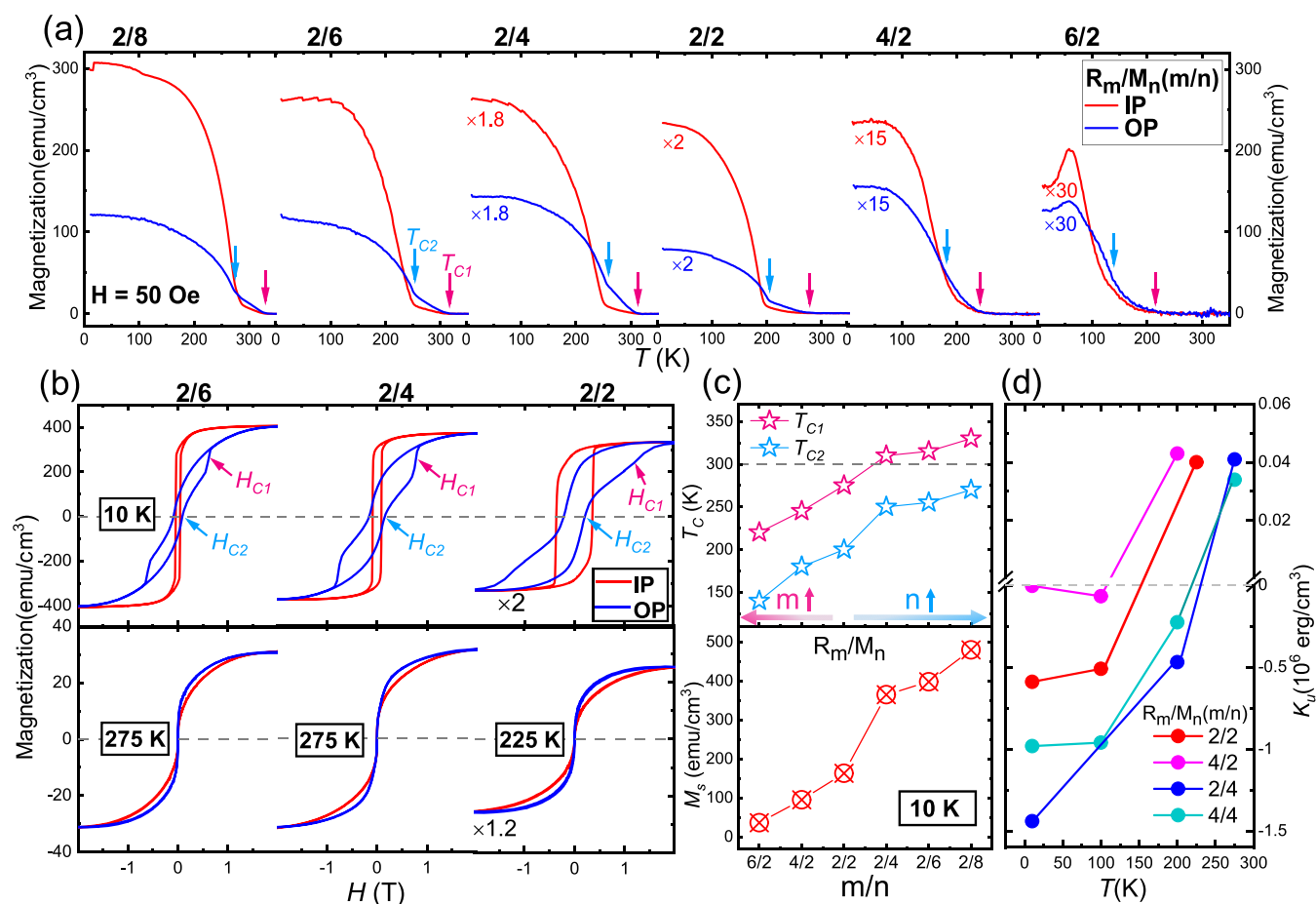
Figure 2. Magnetic Characterization of CRO/LSMO SLs. (a) $M-T$ curves of the R_m/M_n SLs on STO substrates, measured with an in-plane field (red lines) or out-of-plane field (blue lines) of 50 Oe in field-cooling mode. (b) Magnetic hysteresis loops of SLs on STO substrates, measured at 10 K and a temperature between T_{C1} and T_{C2}. The red and blue lines correspond to the in-plane and out-of-plane $M-H$ curves, respectively. (c) Summary of the Curie temperature (T_c) and saturation magnetization (M_s) for the R_m/M_n SLs. (d) Anisotropy constant (K_u) as a function of the temperature (T) for four representative SLs.

giving rise to the emergent FM phase in CRO layer. An obvious advantage of such a CaRuO$_3$ interfacial phase is the enhanced anomalous Hall effect (AHE) in the temperature range of 150−300 K. Compared to the LSMO films, the most promising room-temperature ferromagnetic oxide, the anomalous Hall conductivity σ_{xy}^{AHE} (or anomalous Hall angle θ_H) of the CRO/LSMO superlattices is enhanced by 30 (or 31) times at 150 K and 10 (or 3) times at 300 K, respectively. This work provides a feasible way to create a room-temperature ferromagnetic interfacial phase in originally PM oxides with strong SOC, showing a feasible way toward advanced SOT device design.

RESULTS AND DISCUSSION

Structural Analysis of CRO$_m$/LSMO$_n$ Superlattices. [CRO$_m$/LSMO$_n$]$_{10}$ (R_m/M_n) superlattices (SLs) by alternately stacking CRO (m u.c.) and LSMO (n u.c.) layers with 10 repetitions were epitaxially grown on (001)-oriented STO or (LaAlO$_3$)$_{0.3}$-(Sr$_2$AlTaO$_6$)$_{0.7}$ (LSAT) substrates via pulsed laser deposition. In different SLs, the layer thickness ranges from m = 2, 4, or 6 for CRO and n = 2, 4, 6, or 8 for LSMO. The deposition rate has been carefully calibrated by the small-angle X-ray reflectivity (XRR) technique (see Figure S1, Supporting Information), and the thickness of each sublayer is controlled by the number of laser pulses. Figure 1a, b depicts the X-ray

diffraction (XRD) spectra of the SLs on both STO and LSAT substrates. In addition to the (001) main peak (SL$_0$), distinct satellite peaks (SL$_{\pm1}$, SL$_{\pm2}$, and SL$_{\pm3}$) are observed, indicating good crystallinity and high quality of the SLs. The SL$_0$ peak shifts to higher angles with an increasing CRO layer thickness or decreasing LSMO layer thickness. This is understandable since the lattice constant of CRO is smaller than that of LSMO (3.85 vs 3.87 Å). The decreased separation between satellite peaks with the increase of period thickness (mCRO + nLSMO) is a general feature of the XRD spectra of SLs. To further determine the in-plane strain state, the reciprocal space mapping (RSM) of the (103) reflection is measured. Figure 1c shows the results of the R_2/M_8 SLs on STO and LSAT substrates, which have the largest period thickness in the series. The diffraction spots of the SLs (marked by black arrows) are located just above (below) that of the STO (LSAT) substrate; i.e., the SLs are coherently strained to the substrate without lattice relaxations. The a- and c-axis lattice constants of the SLs are further deduced in Figure 1d. The average c-axis lattice constant of the SLs can be well expressed by the formula $c_{SL} = (m \times c_{CRO} + n \times c_{LSMO})/(m + n)$, where c_{CRO} and c_{LSMO} are lattice constants of the CRO layers and LSMO layers, confirming the ordered SL structure with target thickness.

To obtain atomic-scale structural information, the lattice image of a typical SL R_4/M_6 was captured by using a high-
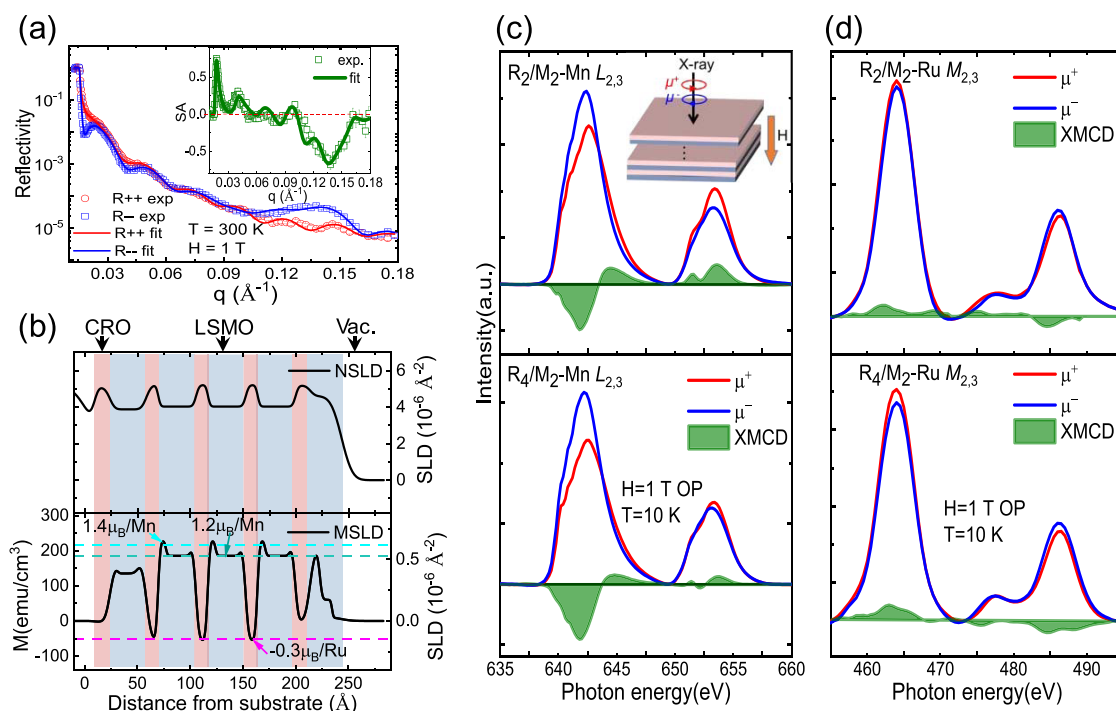
Figure 3. Spatially resolved and elementally resolved magnetic characterization of CRO/LSMO SLs. (a) Reflectivity curves for spin-up (R^{++}) and spin-down (R^{--}) polarized neutrons as a function of wave vector q ($4\pi \sin\theta/\lambda$) measured for the $[R_3/M_9]_5$ SL, where θ is the incident angle and λ is the neutron wavelength. PNR measurements were performed at 300 K under 1 T. The spin asymmetry (SA) was described by $(R^{++} - R^{--})/(R^{++} + R^{--})$ (inset panel). Open symbols and solid lines are experimental data and the results of the best curve fitting, respectively. Error bars represent the standard deviation. (b) Best-fitting model of the structural and magnetic depth profiles for the $[R_3/M_9]_5$ SL. (c) XMCD spectra at the Mn-$L_{2,3}$ edges and (d) Ru $M_{2,3}$ edges of the R_2/M_2 and R_4/M_2 SLs, measured at 10 K with an out-of-plane field of 1 T.

resolution scanning transmission electron microscope (STEM). Figure 1e presents the high-angle annular dark-field (HAADF) image of the cross section of R_4/M_6, taken along the [100] zone axis. Notably, the distinct brightness contrast between the La and Ca atoms highlights the alternating stacking of LSMO and CRO layers, providing clear evidence of the coherent and epitaxial growth of the periodic structure. The line profile analysis along the A- and B-site columns across the interfaces is further shown in the inset panel. The upper CRO/LSMO interface is atomically sharp without visible interlayer mixing. In contrast, partial La^{3+} (or Sr^{2+}) ions in the first La(Sr)−O layer of LSMO near the bottom LSMO/CRO interface are replaced by Ca^{2+} ions, resulting in an A-site intermixing within one-unit cell. This stacking sequence dependence of the interface quality was also observed before in other heterostructures[34,35] and was ascribed to the different surface segregation of heavy and light elements with different ionic radii. This intermixing may slightly affect the properties of the LSMO layer but not the conclusions on the CRO layer given later. All of these results collectively affirm the high quality of SLs with atomically flat interfaces and well-ordered period structures.

Magnetic Characterization. To explore the emergent phenomena in the CRO/LSMO heterostructure, direct magnetic measurements were conducted with the magnetic fields applied along in-plane [100] (IP) and out-of-plane [001] (OP) directions, respectively. Figure 2a compares the IP and OP temperature-dependent magnetization (M−T) curves of two series of SLs: R_2/M_n ($n = 2-8$) and R_m/M_2 ($m = 2-6$), measured under a magnetic field of 50 Oe. The M−T curves measured in higher magnetic fields are given in Figure S2 of

the Supporting Information. The most obvious observation in these M−T curves is the occurrence of two Curie temperatures, especially in the OP M−T curves. Taking the R_2/M_2 SL as an example, as the temperature decreases, the OP M−T curve first exhibits a nearly linear rise of magnetization around 275 K and then a more rapid increase around 200 K. These two inflection points suggest the coexistence of two magnetic phases in the R_2/M_2 SL: phase-1 with a higher FM transition temperature (T_{C1}) and phase-2 with a relatively lower transition temperature (T_{C2}). This multiphase behavior is generally observed in all SLs. Figure S3a presents the dM/dT− T curves of several typical SLs, which show the two transition temperatures more clearly. As summarized in Figure 2c, for the R_2/M_n series of SLs, both T_{C1} and T_{C2} increase with increasing LSMO layer thickness, from 275 and 200 K in the R_2/M_2 SL to 330 and 270 K in the R_2/M_8 SL. Conversely, for the R_m/M_2 series of SLs with the fixed LSMO layer of 2 u.c., T_{C1} and T_{C2} decrease with the increase of CRO layer thickness.

Moreover, the OP and IP M−T curves consistently show a crossover point around the T_{C2}. In the temperature range between T_{C1} and T_{C2}, only phase-1 is in the FM state, causing the magnetization measured with the OP field to surpass that measured with the IP field. Below T_{C2}, with the presence of FM phase-2, the IP curves rapidly overtake the OP curves. This result strongly suggests that FM phase-1 possesses the perpendicular magnetic anisotropy (PMA), while FM phase-2 prefers the in-plane magnetic anisotropy (MA).

To further determine the MA of the R_m/M_n SLs, magnetic-field-dependent magnetization (M−H) curves were measured (Figures 2b and S3b of the Supporting Information) over the temperature range of 10−300 K. At first glance, the OP

hysteresis loops measured at 10 K show two clearly separated coercive fields (H_c), confirming the presence of two FM phases, as suggested by the $M-T$ measurements. After careful analysis, we find that the complex OP $M-H$ curves can be decomposed into two $M-H$ curves (see Figure S4): one representing a hard FM phase and the other a soft FM phase. Taking R_2/M_4 as an example, the hard FM phase with abrupt magnetization transitions at the coercive field (H_c) of ± 0.75 T demonstrates the PMA that should correspond to the FM phase-1 identified from $M-T$ curves. In contrast, the soft FM phase shows a much smoother variation in magnetization with the OP field and a small H_c of ± 0.06 T, suggesting the in-plane MA that corresponds to the FM phase-2 in $M-T$ curves. Based on the different magnetic features of the two phases, we consider FM phase-1, with higher T_C and H_C, to be an interfacial phase, possibly originating from the CRO/LSMO interface coupling. The FM phase-2, with a much smaller H_C, resembles the LSMO bulk phase, which is due to the double exchange interactions between Mn^{3+}/Mn^{4+} ions in the LSMO layers. Naturally, the contribution of FM phase-2 becomes more significant with the increase of LSMO layer thickness. This is exactly what we observed in the $M-H$ curves of the R_2/M_n SLs. The saturation magnetization (M_S) of the SLs, deduced from the $M-H$ curves at 10 K, is depicted in Figure 2c, which shows a similar thickness dependence as the T_C. The M_S of the R_2/M_n SLs rises from $\sim$160 to $\sim$480 emu/cm^3 as the LSMO layer thickness increases from 2 to 8 u.c. This increase is due to the proportional expansion of the LSMO bulk phase, which typically demonstrates a strongly thickness-dependent M_s in the ultrathin case.[36−38] Conversely, the M_s of the R_m/M_2 SLs declines gradually with the increase of CRO layer thickness, possibly due to the weakening of interlayer interaction by the insertion of a PM layer. Moreover, the $M-H$ curves measured at high or low temperatures directly reveal the PMA of the interfacial FM phase (phase-1) or the in-plane MA of the LSMO bulk phase (phase-2), respectively. In the temperature range $T_{C1} < T < T_{C2}$, only the interfacial phase is in the FM state, exhibiting the PMA, as shown in Figure 2b. Conversely, the contribution of the LSMO bulk phase becomes dominant at low temperatures (such as 10 K), causing the SLs to exhibit an in-plane MA. Figure 2d represents the evolution of the anisotropy constant (K_u) with temperature for four typical SLs: R_2/M_2, R_2/M_4, R_4/M_2, and R_4/M_4. Clearly, the K_u is negative (magnetic easy axis along the IP direction) at low temperatures and positive (magnetic easy axis along the out-of-plane direction) at temperatures above T_{C2} of each SL. All of these magnetic measurements suggest that the CRO/LSMO interface coupling has formed an interfacial FM phase with PMA that is distinct from the conventional LSMO bulk phase.

Spatially Resolved and Elementally Resolved Magnetic Characterization. Magnetic measurements clearly reveal the two FM phases in the R_m/M_n SLs, with distinct T_C, H_C, and MA. To investigate the spatial distribution of these two FM phases, polarized neutron reflectometry (PNR) measurements were conducted to reconstruct the magnetic depth profile across the interface. Figure 3a shows the neutron reflectivity of a $[R_3/M_9]_5$ SL as a function of wave vector transfer $q = 4\pi \sin\theta/\lambda$, obtained at 300 K with the neutron spin parallel (R^{++}) or antiparallel (R^{--}) to the applied magnetic field (1 T). Here, θ is the incident angle of the neutron beam, and λ is the neutron wavelength. The inset graph displays the spin asymmetry (SA), defined as SA =

$(R^{++}-R^{--})/(R^{++}+R^{--})$, providing insights into the depth variation of net magnetization across the interface. The best curve fitting for the PNR and SA data in Figure 3a (solid lines) is obtained based on the nuclear scattering length density (nSLD) and magnetic scattering length density (mSLD) models shown in Figure 3b. The spatially resolved mSLD indicates different magnetization values for the interfacial and inner regions of the LSMO layer, approximately 215 emu/cm^3 ($\sim$1.4 μ_B/Mn) and 180 emu/cm^3 ($\sim$1.2 μ_B/Mn), respectively. Notably, the CRO layer also demonstrates an average magnetization of ~ -50 emu/cm^3 (~ -0.3 μ_B/Ru) at 300 K. The positive or negative magnetization values for LSMO or CRO layers indicate that the spins are aligned along or against the applied field. Therefore, the PNR result strongly suggests the antiferromagnetic coupling between the interfacial Ru and Mn ions, possibly originating from the Ru^{4+}-Mn^{4+} antiferromagnetic superexchange interaction, as reported in SRO/LSMO heterojunctions.[39−44] This antiferromagnetic interfacial coupling transfers the magnetic order from the LSMO layer to the adjacent CRO layer, aligning the spins of Ru ions opposite those of Mn ions. Consequently, we consider FM phase-1 to be formed by the strongly magnetically coupled CRO and LSMO interfacial layers, while FM phase-2 corresponds to the inner region of the LSMO layer that retains the properties of LSMO bulk. Naturally, these two FM phases demonstrate distinct magnetic features since they have different origins: the superexchange interactions between interfacial Ru^{4+}-Mn^{4+} ions or the double exchange interactions between Mn^{3+}-Mn^{4+} ions. The enhanced T_C of the interfacial phase as compared to that of the inner phase suggests that the exchange energy of Ru^{4+}-Mn^{4+} ions is even larger than that of the Mn^{3+}-Mn^{4+} ions.

To further confirm the FM order in the CRO layer and its antiferromagnetic alignment with the LSMO layer, we performed XMCD measurements around the Mn-$L_{2,3}$ edge and Ru $M_{2,3}$ edge under an out-of-plane field of 1 T at 10 K. Considering the relatively low intensity of the Ru $M_{2,3}$ edge and the limited penetration depth of X-rays ($\sim$6 nm), here the R_2/M_2 and R_4/M_2 SLs were selected to ensure a reliable Ru $M_{2,3}$ signal. The XMCD spectra were obtained by calculating the differences between the X-ray absorption spectra (XAS) μ^+ and μ^-, where μ^+ and μ^- denote the XAS spectra measured with right-handed and left-handed circularly polarized light, respectively.[45−47] Figure 3c shows the XMCD spectra around the Mn-$L_{2,3}$ edge. As expected, a large dichroism is observed around the Mn edge, indicating a highly spin-polarized state of LSMO. Importantly, a considerable XMCD signal is also detected around the Ru $M_{2,3}$ edge (Figure 3d), suggesting the presence of FM order in the CRO layers. The XMCD signal of the Ru $M_{2,3}$ edge is opposite that of the Mn-$L_{2,3}$ edge, suggesting the antiparallel spin alignment between Ru and Mn ions. This conclusion is also applicable at room temperature, as confirmed by the XMCD results (Figure S6) and the PNR analysis performed at room temperature. All of these results suggest that the CRO layer has been magnetized by the interfacial LSMO layer. These two interfacial layers are antiferromagnetically coupled together, forming the ferromagnetic-like phase-1 with distinct magnetic properties compared with the general LSMO bulk phase. Moreover, the XMCD signal of Mn ions with different magnetic fields H was also studied for the R_2/M_4 SL at 10 K (shown in Figure S7). The Mn-magnetization vs H curve, deduced from the XMCD spectra (for details, see Figure S7), further supports that the
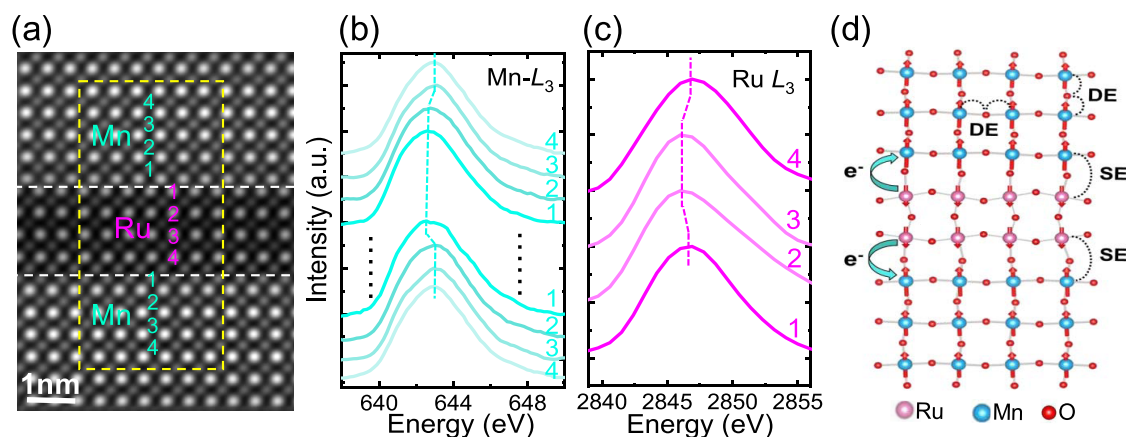
Figure 4. EELS Characterization of CRO/LSMO SLs. (a) Enlarged HAADF image of a local area of the R_4/M_6 SL, where the EELS line profile is conducted in the dashed box along the [001] direction. (b, c) Layer-resolved EELS spectra of the Mn-L_3 edge and Ru-L_3 edge, respectively. (d) Schematic of the CRO/LSMO heterostructure and the interfacial charge transfer, where DE represents double exchange interaction and SE represents superexchange interaction.
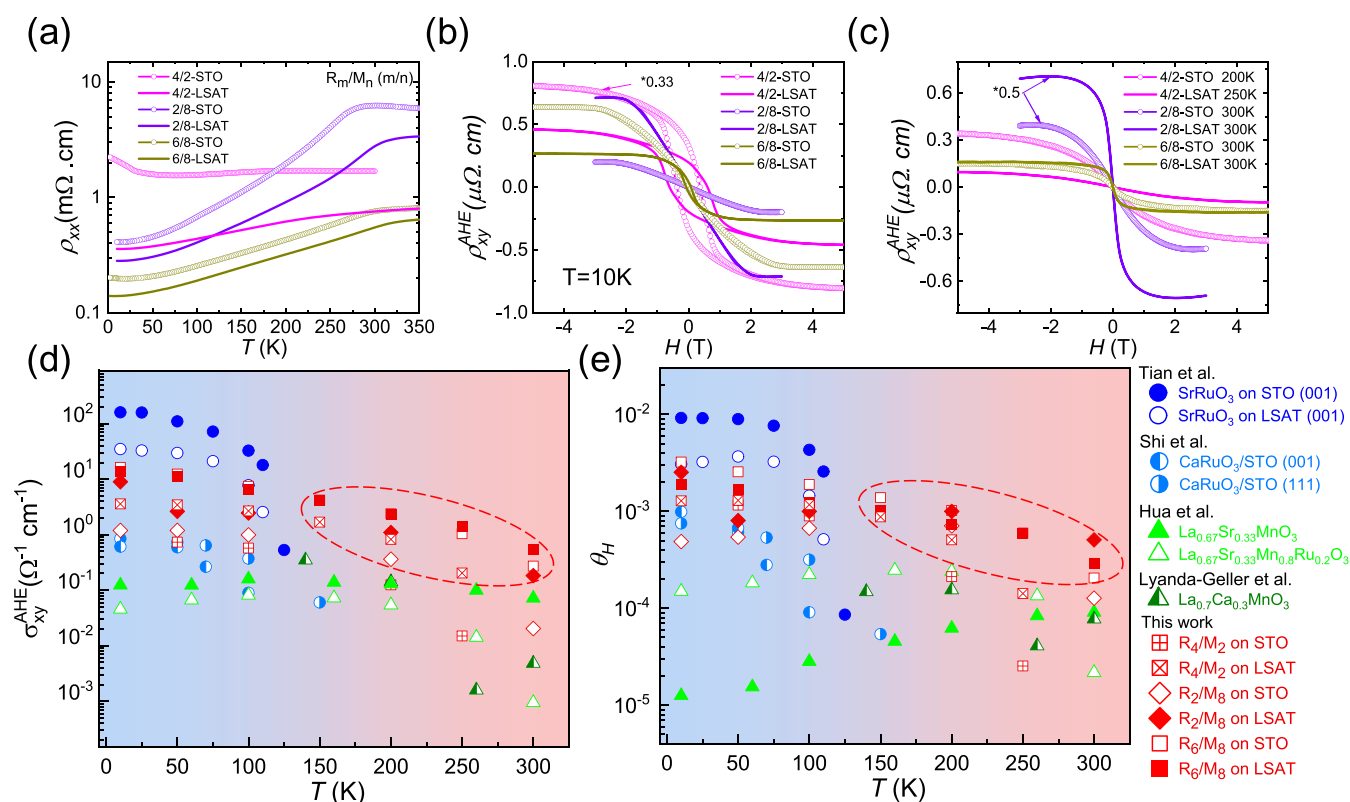

Figure 5. Magneto-transport Characterization of CRO/LSMO SLs. (a) Longitudinal resistivity (ρ_{xx}) versus temperature (T) curves. (b) Anomalous Hall resistivity versus magnetic field ρ_{xy}^{AHE}-H curves at 10 K and (c) temperature near T_{C1} for three representative SLs (R_4/M_2, R_2/M_8, and R_6/M_8) on both STO and LSAT substrates. (d) Saturation anomalous Hall conductivity (σ_{xy}^{AHE}) and (e) anomalous Hall angle (θ_H) as a function of temperature (T) for the R_m/M_n SLs, marked by red symbols. Data of representative magnetic oxides are also presented for comparison. The comparison data are taken from Tian et al.[57] for SrRuO$_3$, from Shi et al.[25,26] for CaRuO$_3$/SrTiO$_3$ SLs, from Hua et al.[59] for La$_{0.67}$Sr$_{0.33}$MnO$_3$ and La$_{0.67}$Sr$_{0.33}$Mn$_{0.8}$Ru$_{0.2}$O$_3$, and from Lyanda-Geller et al.[58] for La$_{0.7}$Ca$_{0.3}$MnO$_3$.

soft FM phase (phase-2) with a small H_c observed in direct magnetic measurement comes from the LSMO bulk phase.

Origin of the Interlayer Coupling at CRO/LSMO Interface. The magnetic measurements described above provide the formation of the emergent interfacial phase in the CRO/LSMO SLs, originating from the superexchange interaction coupling between the interfacial CRO and LSMO layers. In general, such an interlayer coupling is closely related to the charge transfer process across the interface. To gain

more details about the interlayer coupling, layer-resolved electron energy loss spectra (EELS) around the Mn-L_3 and Ru-L_3 edges were further investigated. Figure 4a shows an enlarged HAADF image of a local area of the R_4/M_6 SL, where the EELS line profile is conducted in the dashed box along the [001] direction. As shown in Figure 4b,c, the Mn-L_3 edge exhibits a low-energy shift (from ~643 to 642.6 eV) within one or two Mn−O layers near the interface. Correspondingly, the Ru-L_3 edge in the first one or two Ru−O layers near the

interface shifts to high energies (from ~2846.3 to 2846.7 eV). These opposite energy shifts of Ru and Mn ions highly suggest electron transfer from Ru to Mn at the CRO/LSMO interface, forming a Ru−O−Mn covalent bond. Mn atom is connected with the Ru atom via the apical oxygen, leading to one-to-one hybridization between the respective orbitals, e.g., Ru $t_{2g}xz(yz)$ with Mn $t_{2g}xz(yz)$ and Ru $e_g3z^2 - r^2$ with Mn $e_g3z^2 - r^2$. Obviously, charge transfer occurs preferentially between Ru^{4+} and Mn^{4+} ions since the Fermi level of Mn^{3+} is higher than that of Mn^{4+}. The Ru^{4+} ion has an electron configuration of $t_{2g}^4(3\downarrow,1\uparrow)$, while the Mn^{4+} ion in LSMO has electron configurations of $t_{2g}^3(3\uparrow)$ that corresponds to the half-filled t_{2g} band. Therefore, an antiferromagnetic superexchange interaction is expected between the interfacial Ru and Mn ions according to the Goodenough−Kanamori−Anderson rules (Figure 4d). This is similar to what has been confirmed in SRO/LSMO heterojunctions.[41,44] The strong hybridization between Mn-3d, Ru-4d, and the O-2p orbital and thus the interlayer superexchange interaction would finally induce a high T_C for the interfacial phase. Similar interfacial FM phases with higher transition temperatures than their bulk forms were also observed in other oxide heterostructures. For example, Ueda et al. reported the interfacial ferromagnetism at 375 and 230 K in (111)-oriented 1:1 $LaCrO_3/LaFeO_3$ and $LaMnO_3/LaFeO_3$ superlattices respectively, while the parent bulk materials are all antiferromagnetic.[48,49] Choi et al. reported the high-temperature ferromagnetism up to 410 K in the $BiFeO_3/BiMnO_3$ superlattices, originating from the $Fe^{3+}−O−Mn^{3+}$ superexchange coupling at the interface.[50] Ji et al. reported the interfacial ferromagnetic coupling dramatically increased the Curie temperature of the $LaCoO_3$ film up to 190 K at $LaCoO_3/La_{2/3}Sr_{1/3}MnO_3$ heterostructures.[51]

Additionally, interface charge transfer also increases the proportion of Mn^{3+} ions in the interfacial LSMO layer. Considering the higher spin state of Mn^{3+} ($S = 4$) than that of Mn^{4+} ($S = 3$), the enhanced magnetization in the interfacial LSMO layer compared to that in the inner region can be well explained.

Magneto-Transport Characterization. As mentioned above, the AHE of ferromagnets can significantly enhance the SOT effect, leading to efficient spin injection and spin-charge conversion.[13,16,17] Taniguchi et al. predicted that the spin current excited by AHE has spins aligned along the magnetization (**m**) direction and flows in the **m** × **E** direction, where **E** is the electric field, with the amplitude being proportional to the anomalous Hall conductivity σ_{xy}^{AHE}.[13] However, achieving a large AHE in TMOs at room temperature remains challenging. While 3d LSMO can exhibit a high T_C well above room temperature, its weak SOC results in a small AHE over the whole temperature range. In CRO/LSMO SLs, the FM phase formed by the interlayer coupling between CRO and LSMO can exhibit a T_C exceeding 300 K with apparent PMA. Most importantly, strong SOC is expected in this phase due to the presence of 4d Ru atoms, as already proved by the SOT experiments on ruthenates such as SRO, CRO, and RuO_2.[52−56] The combination of FM and strong SOC at room temperature makes this interfacial phase suitable for potential applications related to AHE and spin-charge conversion.

Figure 5a−c shows the longitudinal resistivity (ρ_{xx}) and anomalous Hall resistivity (ρ_{xy}^{AHE}) of three representative SLs (R_4/M_2, R_2/M_8, and R_6/M_8) on both STO and LSAT substrates. The R_4/M_2 and R_6/M_8 SLs on LSAT exhibit

metallic behavior in the temperature range from 2 to 350 K. The R_2/M_8 SLs exhibit the semiconductive-to-metallic transitions at ~270 K, similar to LSMO bare films. The resistivity of SLs deposited on STO is higher than that of SLs on LSAT, possibly due to the larger tensile strain of STO substrate. The ρ_{xy}^{AHE}-H curves measured at 10 K and a temperature near the T_{C1} of each SL are displayed in Figure 5b,c. Hysteresis- and step-shaped ρ_{xy}^{AHE}-H curves are observed at low and high temperatures, respectively, indicating the establishment of FM order in the SLs. To quantify the AHE, we present the saturation anomalous Hall conductivity σ_{xy}^{AHE} and anomalous Hall angle θ_H as functions of temperature T for above SLs (marked with red symbols in Figure 5d,e), where $\sigma_{xy}^{AHE} = \rho_{xy}^{AHE}/\rho_{xx}^2$ and $\theta_H = \rho_{xy}^{AHE}/\rho_{xx}$. For comparison, data from representative ruthenium oxides (SRO film, CRO/STO SL) and manganese oxides (LCMO, LSMO, and Ru-doped LSMO films) are also included.[57,25,26,58,59] The σ_{xy}^{AHE} and θ_H of CRO/LSMO SLs are not superior to those of SRO below 100 K. However, the σ_{xy}^{AHE} and θ_H of SRO decrease dramatically when the temperature exceeds 100 K and finally diminish at temperatures above its T_C of ~150 K. In contrast, the σ_{xy}^{AHE} and θ_H of the CRO/LSMO SLs can be maintained up to 300 K. The largest σ_{xy}^{AHE} and θ_H values, ~ 4.1 $\Omega^{-1}\cdot cm^{-1}$ and 0.14% at 150 K, and ~0.53 $\Omega^{-1}\cdot cm^{-1}$ and 0.02% at 300 K, are obtained in the R_6/M_8 SLs. Notably, the AHE of the SL samples is superior to that of LSMO or LCMO films in the whole temperature range. The largest enhancement rate of σ_{xy}^{AHE} (or θ_H) for our CRO/LSMO SLs, compared to LSMO films, is ~100 (or 300) at 2 K, ~30 (or 31) at 150 K, and ~10 (or 3) at 300 K. Previous work has reported that Ru doping in LSMO films can enhance the anomalous Hall resistivity ρ_{xy}^{AHE} at room temperature.[53] However, random Ru doping severely deteriorates the longitudinal conductivity ρ_{xx}, resulting in even lower σ_{xy}^{AHE} than that of bare LSMO films. Unlike the doping method, here, the SOC effect in the CRO/LSMO SLs is induced by inserting ultrathin CRO layers between LSMO layers with atomically flat interfaces, which slightly affects the metallic conduction of either CRO or LSMO. Thus, significant improvements of σ_{xy}^{AHE} and θ_H are achieved in the SL structure.

CONCLUSIONS

In summary, we successfully achieved a room-temperature FM interfacial phase with a strong SOC in the CRO/LSMO superlattices. Magnetic characterization displays that the interfacial phase possesses PMA, distinct from the inner LSMO phase that prefers in-plane MA. The PNR and XMCD results reveal that the CRO layers do exhibit ferromagnetism at room temperature, with an average magnetic moment of ~0.3 μ_B/Ru. Additionally, the CRO layer is antiferromagnetically coupled with the LSMO layer at the interface due to the $Ru^{4+}−Mn^{4+}$ superexchange interaction. EELS analysis suggests a notable charge transfer from Ru to Mn at the interface, which increases the proportion of Mn^{3+} ions in the interfacial region of the LSMO layer and thus enhances the magnetization in the interfacial region of the LSMO layer compared to the inner region. Notably, in the temperature range of 150−300 K, the anomalous Hall conductivity and anomalous Hall angle of the CRO/LSMO SLs are significantly larger than that of LSMO bare films. The largest enhancement rate of σ_{xy}^{AHE} (θ_H) is ~30 (31) at 150 K and ~10 (3) at 300 K. This work provides a feasible way to fabricate a room-temperature ferromagnetic interfacial phase with strong SOC and reliability of oxide-based spintronic devices.

METHODS

Sample Synthesis. High-quality R_m/M_n SLs were epitaxially grown on single-crystalline (001)-oriented STO and LSAT substrates by pulsed laser deposition (KrF, λ = 248 nm) with 10 repetitions, where m and n represent the thickness of CRO and LSMO sublayers, ranging from 2 to 8 u.c. During the growth process, the substrate was kept at 680 °C, and the oxygen pressure was set to 40 Pa. The fluence of the laser pulse was 1.2 J/cm², with a repetition rate of 2 Hz. After deposition, the sample was cooled to room temperature under an oxygen pressure of 100 Pa. The deposition rate of each film was carefully calibrated by the technique of small-angle X-ray reflectivity (XRR), and the thickness of the sublayers was precisely controlled by counting the pulse number.

Sample Characterization. The surface morphology was measured with an atomic force microscope (AFM) (SPI 3800N, Seiko). The crystal structure was determined with a high-resolution X-ray diffractometer (D8 Discover, Bruker) with Cu Kα radiation. Atomic-scale lattice images were recorded by high-resolution scanning transmission electron microscopy (STEM) with double CS correctors (Thermo Fisher Spectra 300). Cross-sectional thin samples for STEM analysis were prepared using a dual-beam focused ion beam system along the [100] direction. The magnetic properties were measured by a Quantum Design vibrating sample magnetometer (VSM-SQUID) in the temperature range of 10−350 K. The transport measurements were performed in a Quantum Design physical property measurement system (PPMS) with standard Hall bar geometry. The Hall bar devices, fabricated by conventional lithography and Ar-ion etching techniques, have a width of 200 μm and a length of 1200 μm. Aluminum wires, 20 μm in diameter, were employed to establish the connections between the sample and the electrodes via ultrasound-assisted wire bonding. DC current of 100 μA was applied along the in-plane [100] direction, and the magnetic field was applied along the out-of-plane [001] direction.

Polarized Neutron Reflectometry (PNR). PNR experiments were conducted at the MR beamline of the Chinese Spallation Neutron Source (CSNS). The samples were field-cooled and measured at 1 T along the in-plane direction. PNR measurements were carried out at 300 K in the specular reflection geometry with wave vector transfer (q) perpendicular to the surface plane. The neutron reflectivity was recorded as a function of q for the spin-up (R^{++}) and spin-down (R^{--}) polarized neutrons. These neutron reflectivities were normalized to the asymptotic value of the Fresnel reflectivity ($R_F = 16\pi^2/q^4$) for a better illustration. The difference between R^{++} and R^{--} was calculated as the spin asymmetry $SA = \frac{(R^{++} - R^{--})}{(R^{++} + R^{--})}$. The PNR data were fitted using GenX software.

X-ray Magnetic Circular Dichroism (XMCD) Spectroscopy. The X-ray absorption spectroscopy (XAS) and magnetic dichroism (XMCD) experiments at the Mn-$L_{2,3}$ and Ru $M_{2,3}$ edges were carried out at Beamline BL08U1A and BL07U of the Shanghai Synchrotron Radiation Facility (SSRF). The measurements were performed at 10 K using total-electron-yield mode. Both the incident circularly polarized X-ray beam and magnetic field were normal to the sample surface. The XMCD spectra were obtained as the difference of the XAS spectra μ^+ and μ^-, where μ^+ and μ^- denote the XAS spectra measured with right-handed and left-handed circularly polarized light, respectively.

ASSOCIATED CONTENT

ⓢ Supporting Information

The Supporting Information is available free of charge at https://pubs.acs.org/doi/10.1021/acsnano.4c10014.

The atomic force microscope and XRR of the R_2/M_6 SL, the $M-T$, dM/dT-T, and $M-H$ curves for several typical SLs, three fitting models of PNR, XAS, and XMCD spectra at the Mn-$L_{2,3}$ edges and Ru $M_{2,3}$ edges of the R_2/M_4 SL, and anomalous Hall resistivity (ρ_{xy}^{AHE}) versus magnetic field (H) for three representative SLs (R_4/M_2, R_2/M_8, and R_6/M_8) on both STO and LSAT substrates (PDF)

AUTHOR INFORMATION

Corresponding Authors

Yuansha Chen − *Beijing National Laboratory for Condensed Matter Physics and Institute of Physics, Chinese Academy of Sciences, Beijing 100190, China; School of Physical Sciences, University of Chinese Academy of Sciences, Beijing 100049, China*; Email: yschen@iphy.ac.cn

Tao Zhu − *Beijing National Laboratory for Condensed Matter Physics and Institute of Physics, Chinese Academy of Sciences, Beijing 100190, China; Spallation Neutron Source Science Center, Dongguan 523803, China*; Email: tzhu@iphy.ac.cn

Jirong Sun − *Beijing National Laboratory for Condensed Matter Physics and Institute of Physics, Chinese Academy of Sciences, Beijing 100190, China; School of Physical Sciences, University of Chinese Academy of Sciences, Beijing 100049, China;* ⓞ orcid.org/0000-0003-4531-4794; Email: jrsun@iphy.ac.cn

Authors

Jie Zheng − *Beijing National Laboratory for Condensed Matter Physics and Institute of Physics, Chinese Academy of Sciences, Beijing 100190, China; School of Physical Sciences, University of Chinese Academy of Sciences, Beijing 100049, China*

Jing Zhang − *Songshan Lake Materials Laboratory, Dongguan, Guangdong 523808, China*

Sheng Cheng − *Spallation Neutron Source Science Center, Dongguan 523803, China*

Wenxiao Shi − *Beijing National Laboratory for Condensed Matter Physics and Institute of Physics, Chinese Academy of Sciences, Beijing 100190, China; School of Physical Sciences, University of Chinese Academy of Sciences, Beijing 100049, China*

Mengqin Wang − *Beijing National Laboratory for Condensed Matter Physics and Institute of Physics, Chinese Academy of Sciences, Beijing 100190, China; School of Physical Sciences, University of Chinese Academy of Sciences, Beijing 100049, China*

Zhe Li − *Beijing National Laboratory for Condensed Matter Physics and Institute of Physics, Chinese Academy of Sciences, Beijing 100190, China; School of Physical Sciences, University of Chinese Academy of Sciences, Beijing 100049, China*

Yunzhong Chen − *Beijing National Laboratory for Condensed Matter Physics and Institute of Physics, Chinese Academy of Sciences, Beijing 100190, China; School of Physical Sciences, University of Chinese Academy of Sciences, Beijing 100049, China;* ⓞ orcid.org/0000-0001-8368-5823

Fengxia Hu − *Beijing National Laboratory for Condensed Matter Physics and Institute of Physics, Chinese Academy of Sciences, Beijing 100190, China; School of Physical Sciences, University of Chinese Academy of Sciences, Beijing 100049, China; Songshan Lake Materials Laboratory, Dongguan, Guangdong 523808, China;* ⓞ orcid.org/0000-0003-0383-0213

Baogen Shen − *Beijing National Laboratory for Condensed Matter Physics and Institute of Physics, Chinese Academy of Sciences, Beijing 100190, China; School of Physical Sciences, University of Chinese Academy of Sciences, Beijing 100049, China; Ningbo Institute of Materials Technology &*

Engineering, Chinese Academy of Sciences, Ningbo, Zhejiang 315201, China; Ganjiang Innovation Academy, Chinese Academy of Sciences, Ganzhou, Jiangxi 341000, China;
orcid.org/0000-0003-4819-1806

Complete contact information is available at:
https://pubs.acs.org/10.1021/acsnano.4c10014

Author Contributions
[∇]J. Zheng and J. Zhang contributed equally to this work.

Notes
The authors declare no competing financial interest.

REFERENCES

(1) Berger, L. Exchange Interaction between Ferromagnetic Domain Wall and Electric Current in Very Thin Metallic Films. *J. Appl. Phys.* **1984**, *55* (6), 1954−1956.

(2) Slonczewski, J. C. Current-Driven Excitation of Magnetic Multilayers. *J. Magn. Magn. Mater.* **1996**, *159* (1−2), L1−L7.

(3) Ralph, D. C.; Stiles, M. D. Spin Transfer Torques. *J. Magn. Magn. Mater.* **2008**, *320* (7), 1190−1216.

(4) Miron, I. M.; Garello, K.; Gaudin, G.; Zermatten, P. J.; Costache, M. V.; Auffret, S.; Bandiera, S.; Rodmacq, B.; Schuhl, A.; Gambardella, P. Perpendicular Switching of a Single Ferromagnetic Layer Induced by In-Plane Current Injection. *Nature* **2011**, *476* (7359), 189−193.

(5) Liu, L.; Pai, C.-F.; Li, Y.; Tseng, H. W.; Ralph, D. C.; Buhrman, R. A. Spin-Torque Switching with the Giant Spin Hall Effect of Tantalum. *Science* **2012**, *336* (6081), 555−558.

(6) Garello, K.; Miron, I. M.; Avci, C. O.; Freimuth, F.; Mokrousov, Y.; Blügel, S.; Auffret, S.; Boulle, O.; Gaudin, G.; Gambardella, P. Symmetry and Magnitude of Spin-Orbit Torques in Ferromagnetic Heterostructures. *Nat. Nanotechnol.* **2013**, *8* (8), 587−593.

(7) Fan, X.; Celik, H.; Wu, J.; Ni, C.; Lee, K.-J.; Lorenz, V. O.; Xiao, J. Q. Quantifying Interface and Bulk Contributions to Spin-Orbit Torque in Magnetic Bilayers. *Nat. Commun.* **2014**, *5* (1), No. 3042.

(8) Fukami, S.; Zhang, C.; DuttaGupta, S.; Kurenkov, A.; Ohno, H. Magnetization Switching by Spin-Orbit Torque in an Antiferromagnet−Ferromagnet Bilayer System. *Nat. Mater.* **2016**, *15* (5), 535−541.

(9) Hirsch, J. E. Spin Hall Effect. *Phys. Rev. Lett.* **1999**, *83* (9), 1834−1837.

(10) Sinova, J.; Valenzuela, S. O.; Wunderlich, J.; Back, C. H.; Jungwirth, T. Spin Hall Effects. *Rev. Mod. Phys.* **2015**, *87* (4), 1213−1260.

(11) Liu, L.; Lee, O. J.; Gudmundsen, T. J.; Ralph, D. C.; Buhrman, R. A. Current-Induced Switching of Perpendicularly Magnetized Magnetic Layers Using Spin Torque from the Spin Hall Effect. *Phys. Rev. Lett.* **2012**, *109* (9), No. 096602.

(12) Ando, K.; Takahashi, S.; Harii, K.; Sasage, K.; Ieda, J.; Maekawa, S.; Saitoh, E. Electric Manipulation of Spin Relaxation Using the Spin Hall Effect. *Phys. Rev. Lett.* **2008**, *101* (3), No. 036601.

(13) Taniguchi, T.; Grollier, J.; Stiles, M. D. Spin-Transfer Torques Generated by the Anomalous Hall Effect and Anisotropic Magnetoresistance. *Phys. Rev. Appl.* **2015**, *3* (4), No. 044001.

(14) Baek, S.-h.; Amin, V. P.; Oh, Y.-W.; Go, G.; Lee, S.-J.; Lee, G.-H.; Kim, K.-J.; Stiles, M. D.; Park, B.-G.; Lee, K.-J. Spin Currents and Spin-Orbit Torques in Ferromagnetic Trilayers. *Nat. Mater.* **2018**, *17* (6), 509−513.

(15) Fukami, S.; Anekawa, T.; Zhang, C.; Ohno, H. A Spin−Orbit Torque Switching Scheme with Collinear Magnetic Easy Axis and Current Configuration. *Nat. Nanotechnol.* **2016**, *11* (7), 621−625.

(16) Iihama, S.; Taniguchi, T.; Yakushiji, K.; Fukushima, A.; Shiota, Y.; Tsunegi, S.; Hiramatsu, R.; Yuasa, S.; Suzuki, Y.; Kubota, H. Spin-Transfer Torque Induced by the Spin Anomalous Hall Effect. *Nat. Electron.* **2018**, *1* (2), 120−123.

(17) Hibino, Y.; Taniguchi, T.; Yakushiji, K.; Fukushima, A.; Kubota, H.; Yuasa, S. Giant Charge-to-Spin Conversion in Ferromagnet via Spin-Orbit Coupling. *Nat. Commun.* **2021**, *12* (1), No. 6254.

(18) Cao, G.; McCall, S.; Shepard, M.; Crow, J. E.; Guertin, R. P. Thermal, Magnetic, and Transport Properties of Single-Crystal $Sr_{1-x}Ca_xRuO_3$ ($0 \leq x \leq 1.0$). *Phys. Rev. B* **1997**, *56* (1), No. 321.

(19) Shepard, M.; McCall, S.; Cao, G.; Crow, J. E. Thermodynamic Properties of Perovskite $ARuO_3$ (A = Ca, Sr, and Ba) Single Crystals. *J. Appl. Phys.* **1997**, *81* (8), 4978−4980.

(20) Zeb, M. A.; Kee, H.-Y. Interplay between Spin-Orbit Coupling and Hubbard Interaction in $SrIrO_3$ and Related *Pbnm* Perovskite Oxides. *Phys. Rev. B* **2012**, *86* (8), No. 085149.

(21) Nie, Y. F.; King, P. D. C.; Kim, C. H.; Uchida, M.; Wei, H. I.; Faeth, B. D.; Ruf, J. P.; Ruff, J. P. C.; Xie, L.; Pan, X.; Fennie, C. J.; Schlom, D. G.; Shen, K. M. Interplay of Spin-Orbit Interactions, Dimensionality, and Octahedral Rotations in Semimetallic $SrIrO_3$. *Phys. Rev. Lett.* **2015**, *114* (1), No. 016401.

(22) Masuko, M.; Fujioka, J.; Nakamura, M.; Kawasaki, M.; Tokura, Y. Strain-Engineering of Charge Transport in the Correlated Dirac Semimetal of Perovskite $CaIrO_3$ Thin Films. *APL Mater.* **2019**, *7* (8), No. 081115.

(23) Lin, W.; Liu, L.; Liu, Q.; Li, L.; Shu, X.; Li, C.; Xie, Q.; Jiang, P.; Zheng, X.; Guo, R.; Lim, Z.; Zeng, S.; Zhou, G.; Wang, H.; Zhou, J.; Yang, P.; Ariando; Pennycook, S. J.; Xu, X.; Zhong, Z.; Wang, Z.; Chen, J. Electric Field Control of the Magnetic Weyl Fermion in an Epitaxial $SrRuO_3$ (111) Thin Film. *Adv. Mater.* **2021**, *33* (36), No. 2101316.

(24) Li, Z.; Shen, S.; Tian, Z.; Hwangbo, K.; Wang, M.; Wang, Y.; Bartram, F. M.; He, L.; Lyu, Y.; Dong, Y.; Wan, G.; Li, H.; Lu, N.; Zang, J.; Zhou, H.; Arenholz, E.; He, Q.; Yang, L.; Luo, W.; Yu, P. Reversible Manipulation of the Magnetic State in $SrRuO_3$ through Electric-Field Controlled Proton Evolution. *Nat. Commun.* **2020**, *11* (1), No. 184.

(25) Shi, W.; Zhang, J.; Chen, X.; Zhang, Q.; Zhan, X.; Li, Z.; Zheng, J.; Wang, M.; Han, F.; Zhang, H.; Gu, L.; Zhu, T.; Liu, B.; Chen, Y.; Hu, F.; Shen, B.; Chen, Y.; Sun, J. Symmetry-Mismatch-Induced Ferromagnetism in the Interfacial Layers of $CaRuO_3/SrTiO_3$ Superlattices. *Adv. Funct. Mater.* **2023**, *33* (22), No. 2300338.

(26) Shi, W.; Zheng, J.; Li, Z.; Wang, M.; Zhu, Z.; Zhang, J.; Zhang, H.; Chen, Y.; Hu, F.; Shen, B.; Chen, Y.; Sun, J. Enhancing Interfacial Ferromagnetism and Magnetic Anisotropy of $CaRuO_3$/$SrTiO_3$ Superlattices via Substrate Orientation. *Small* **2024**, *20* (17), No. 2308172.

(27) Yang, J.; Suwa, H.; Meyers, D.; Zhang, H.; Horak, L.; Wang, Z.; Fabbris, G.; Choi, Y.; Karapetrova, J.; Kim, J.-W.; Haskel, D.; Ryan, P. J.; Dean, M. P. M.; Hao, L.; Liu, J. Quasi-Two-Dimensional Anomalous Hall Mott Insulator of Topologically Engineered $J_{Eff} = 1/2$ Electrons. *Phys. Rev. X* **2022**, *12* (3), No. 031015.

(28) Skoropata, E.; Nichols, J.; Ok, J. M.; Chopdekar, R. V.; Choi, E. S.; Rastogi, A.; Sohn, C.; Gao, X.; Yoon, S.; Farmer, T.; Desautels, R. D.; Choi, Y.; Haskel, D.; Freeland, J. W.; Okamoto, S.; Brahlek, M.;

Lee, H. N. Interfacial Tuning of Chiral Magnetic Interactions for Large Topological Hall Effects in LaMnO₃/SrIrO₃ Heterostructures. *Sci. Adv.* **2020**, *6* (27), No. eaaz3902.

(29) Jaiswal, A. K.; Wang, D.; Wollersen, V.; Schneider, R.; Tacon, M. L.; Fuchs, D. Direct Observation of Strong Anomalous Hall Effect and Proximity-Induced Ferromagnetic State in SrIrO₃. *Adv. Mater.* **2022**, *34* (14), No. 2109163.

(30) Nichols, J.; Gao, X.; Lee, S.; Meyer, T. L.; Freeland, J. W.; Lauter, V.; Yi, D.; Liu, J.; Haskel, D.; Petrie, J. R.; Guo, E. J.; Herklotz, A.; Lee, D.; Ward, T. Z.; Eres, G.; Fitzsimmons, M. R.; Lee, H. N. Emerging Magnetism and Anomalous Hall Effect in Iridate−Manganite Heterostructures. *Nat. Commun.* **2016**, *7* (1), No. 12721.

(31) Anderson, P. W. Antiferromagnetism. Theory of Superexchange Interaction. *Phys. Rev.* **1950**, *79* (2), No. 350.

(32) Goodenough, J. B. Theory of the Role of Covalence in the Perovskite-Type Manganites [La, M(II)]MnO₃. *Phys. Rev.* **1955**, *100* (2), No. 564.

(33) Kanamori, J. Superexchange Interaction and Symmetry Properties of Electron Orbitals. *J. Phys. Chem. Solids* **1959**, *10* (2−3), 87−98.

(34) Nakagawa, N.; Hwang, H. Y.; Muller, D. A. Why Some Interfaces Cannot Be Sharp. *Nat. Mater.* **2006**, *5* (3), 204−209.

(35) Gibert, M.; Viret, M.; Torres-Pardo, A.; Piamonteze, C.; Zubko, P.; Jaouen, N.; Tonnerre, J.-M.; Mougin, A.; Fowlie, J.; Catalano, S.; Gloter, A.; Stéphan, O.; Triscone, J.-M. Interfacial Control of Magnetic Properties at LaMnO₃/LaNiO₃ Interfaces. *Nano Lett.* **2015**, *15* (11), 7355−7361.

(36) Liao, Z.; Gauquelin, N.; Green, R. J.; Macke, S.; Gonnissen, J.; Thomas, S.; Zhong, Z.; Li, L.; Si, L.; Van Aert, S.; Hansmann, P.; Held, K.; Xia, J.; Verbeeck, J.; Van Tendeloo, G.; Sawatzky, G. A.; Koster, G.; Huijben, M.; Rijnders, G. Thickness Dependent Properties in Oxide Heterostructures Driven by Structurally Induced Metal−Oxygen Hybridization Variations. *Adv. Funct. Mater.* **2017**, *27* (17), No. 1606717.

(37) Lepetit, M.-B.; Mercey, B.; Simon, C. Interface Effects in Perovskite Thin Films. *Phys. Rev. Lett.* **2012**, *108* (8), No. 087202.

(38) Kourkoutis, L. F.; Song, J. H.; Hwang, H. Y.; Muller, D. A. Microscopic Origins for Stabilizing Room-Temperature Ferromagnetism in Ultrathin Manganite Layers. *Proc. Natl. Acad. Sci. U.S.A.* **2010**, *107* (26), 11682−11685.

(39) Ke, X.; Rzchowski, M. S.; Belenky, L. J.; Eom, C. B. Positive Exchange Bias in Ferromagnetic La₀.₆₇Sr₀.₃₃MnO₃/SrRuO₃ Bilayers. *Appl. Phys. Lett.* **2004**, *84* (26), 5458−5460.

(40) Ziese, M.; Vrejoiu, I.; Hesse, D. Inverted Hysteresis and Giant Exchange Bias in La₀.₇Sr₀.₃MnO₃/SrRuO₃ Superlattices. *Appl. Phys. Lett.* **2010**, *97* (5), No. 052504.

(41) Qin, Q.; He, S.; Lin, W.; Yoong, H. Y.; Liu, L.; Li, M.; Pennycook, S. J.; Xiao, W.; Yang, P.; Song, W.; Chen, J. Interfacial Antiferromagnetic Coupling between SrRuO₃ and La₀.₇Sr₀.₃MnO₃ with Orthogonal Easy Axis. *Phys. Rev. Mater.* **2018**, *2* (10), No. 104405.

(42) Das, S.; Herklotz, A.; Pippel, E.; Guo, E.-J.; Rata, D.; Dörr, K. Strain Dependence of Antiferromagnetic Interface Coupling in La₀.₇Sr₀.₃MnO₃/SrRuO₃ Superlattices. *Phys. Rev. B* **2015**, *91* (13), No. 134405.

(43) Seo, J. W.; Prellier, W.; Padhan, P.; Boullay, P.; Kim, J.-Y.; Lee, H.; Batista, C. D.; Martin, I.; Chia, E. E. M.; Wu, T.; Cho, B.-G.; Panagopoulos, C. Tunable Magnetic Interaction at the Atomic Scale in Oxide Heterostructures. *Phys. Rev. Lett.* **2010**, *105* (16), No. 167206.

(44) Ziese, M.; Vrejoiu, I.; Pippel, E.; Esquinazi, P.; Hesse, D.; Etz, C.; Henk, J.; Ernst, A.; Maznichenko, I. V.; Hergert, W.; Mertig, I. Tailoring Magnetic Interlayer Coupling in La₀.₇Sr₀.₃MnO₃/SrRuO₃ Superlattices. *Phys. Rev. Lett.* **2010**, *104* (16), No. 167203.

(45) Zhang, J.; Cheng, L.; Cao, H.; Bao, M.; Zhao, J.; Liu, X.; Zhao, A.; Choi, Y.; Zhou, H.; Shafer, P.; Zhai, X. The Exceedingly Strong Two-Dimensional Ferromagnetism in Bi-Atomic Layer SrRuO₃ with a Critical Conduction Transition. *Nano Res.* **2022**, *15* (8), 7584−7589.

(46) Okamoto, J.; Okane, T.; Saitoh, Y.; Terai, K.; Fujimori, S.-I.; Muramatsu, Y.; Yoshii, K.; Mamiya, K.; Koide, T.; Fujimori, A.; Fang, Z.; Takeda, Y.; Takano, M. Soft X-Ray Magnetic Circular Dichroism Study of Ca₁₋ₓSrₓRuO₃ across the Ferromagnetic Quantum Phase Transition. *Phys. Rev. B* **2007**, *76* (18), No. 184441.

(47) Terai, K.; Yoshii, K.; Takeda, Y.; Fujimori, S. I.; Saitoh, Y.; Ohwada, K.; Inami, T.; Okane, T.; Arita, M.; Shimada, K.; Namatame, H.; Taniguchi, M.; Kobayashi, K.; Kobayashi, M.; Fujimori, A. X-Ray Magnetic Circular Dichroism and Photoemission Studies of Ferromagnetism in CaMn₁₋ₓRuₓO₃ Thin Films. *Phys. Rev. B* **2008**, *77* (11), No. 115128.

(48) Ueda, K.; Tabata, H.; Kawai, T. Ferromagnetism in LaFeO₃-LaCrO₃ Superlattices. *Science* **1998**, *280* (5366), 1064−1066.

(49) Ueda, K.; Tabata, H.; Kawai, T. Atomic Arrangement and Magnetic Properties of LaFeO₃− LaMnO₃ Artificial Superlattices. *Phys. Rev. B* **1999**, *60* (18), No. R12561.

(50) Choi, E.-M.; Kleibeuker, J. E.; Fix, T.; Xiong, J.; Kinane, C. J.; Arena, D.; Langridge, S.; Chen, A.; Bi, Z.; Lee, J. H.; Wang, H.; Jia, Q.; Blamire, M. G.; MacManus-Driscoll, J. L. Interface-Coupled BiFeO₃/BiMnO₃ Superlattices with Magnetic Transition Temperature up to 410 K. *Adv. Mater. Interfaces* **2016**, *3* (5), No. 1500597.

(51) Ji, Y.; Hu, S.; Liu, J.; Wei, L.; Luo, C.; Ukleev, V.; Radu, F.; Yan, W.; Chen, D.; Zhong, Z.; Gan, Y.; Chen, K.; Liao, Z. High-Temperature Ferromagnetic LaCoO₃ Triggered by Interfacial Electron Transfer and Exchange Coupling. *Phys. Rev. B* **2024**, *109* (17), No. 174423.

(52) Ou, Y.; Wang, Z.; Chang, C. S.; Nair, H. P.; Paik, H.; Reynolds, N.; Ralph, D. C.; Muller, D. A.; Schlom, D. G.; Buhrman, R. A. Exceptionally High, Strongly Temperature Dependent, Spin Hall Conductivity of SrRuO₃. *Nano Lett.* **2019**, *19* (6), 3663−3670.

(53) Zhou, J.; Shu, X.; Lin, W.; Shao, D. F.; Chen, S.; Liu, L.; Yang, P.; Tsymbal, E. Y.; Chen, J. Modulation of Spin-Orbit Torque from SrRuO₃ by Epitaxial-Strain-Induced Octahedral Rotation. *Adv. Mater.* **2021**, *33* (30), No. 2007114.

(54) Wei, J.; Zhong, H.; Liu, J.; Wang, X.; Meng, F.; Xu, H.; Liu, Y.; Luo, X.; Zhang, Q.; Guang, Y.; Feng, J.; Zhang, J.; Yang, L.; Ge, C.; Gu, L.; Jin, K.; Yu, G.; Han, X. Enhancement of Spin-Orbit Torque by Strain Engineering in SrRuO₃ Films. *Adv. Funct. Mater.* **2021**, *31* (40), No. 2100380.

(55) Bai, H.; Zhang, Y. C.; Zhou, Y. J.; Chen, P.; Wan, C. H.; Han, L.; Zhu, W. X.; Liang, S. X.; Su, Y. C.; Han, X. F.; Pan, F.; Song, C. Efficient Spin-to-Charge Conversion via Alternagnetic Spin Splitting Effect in Antiferromagnet RuO₂. *Phys. Rev. Lett.* **2023**, *130* (21), No. 216701.

(56) Zhang, Y.; Bai, H.; Han, L.; Chen, C.; Zhou, Y.; Back, C. H.; Pan, F.; Wang, Y.; Song, C. Simultaneous High Charge-Spin Conversion Efficiency and Large Spin Diffusion Length in Alternagnetic RuO₂. *Adv. Funct. Mater.* **2024**, *34* (24), No. 2313332.

(57) Tian, D.; Liu, Z.; Shen, S.; Li, Z.; Zhou, Y.; Liu, H.; Chen, H.; Yu, P. Manipulating Berry Curvature of SrRuO₃ Thin Films via Epitaxial Strain. *Proc. Natl. Acad. Sci. U.S.A.* **2021**, *118* (18), No. e2101946118.

(58) Lyanda-Geller, Y.; Chun, S. H.; Salamon, M. B.; Goldbart, P. M.; Han, P. D.; Tomioka, Y.; Asamitsu, A.; Tokura, Y. Charge Transport in Manganites: Hopping Conduction, the Anomalous Hall Effect, and Universal Scaling. *Phys. Rev. B* **2001**, *63* (18), No. 184426.

(59) Hua, E.; Si, L.; Dai, K.; Wang, Q.; Ye, H.; Liu, K.; Zhang, J.; Lu, J.; Chen, K.; Jin, F.; Wang, L.; Wu, W. Ru-Doping-Induced Spin Frustration and Enhancement of the Room-Temperature Anomalous Hall Effect in La₂/₃Sr₁/₃MnO₃ Films. *Adv. Mater.* **2022**, *34* (47), No. 2206685.